Science of the Total Environment 627 (2018) 1473–1484

Contents lists available at ScienceDirect

Science of the Total Environment

journal homepage: www.elsevier.com/locate/scitotenv

2015–16 floods and droughts in China, and its response to the strong El Niño

Feng Ma [a], Aizhong Ye [a,*], Jinjun You [b], Qingyun Duan [a]

[a] State Key Laboratory of Earth Surface and Ecological Resources, Faculty of Geographical Science, Beijing Normal University, Beijing 100875, China
[b] State Key Laboratory of Simulation and Regulation of Water Cycle in River Basin, China Institute of Water Resources and Hydropower Research, Beijing 100038, China

HIGHLIGHTS

- Flood and drought in China were sensitive to the evolution of the 2015–16 El Niño.
- Hydro-climate anomalies of 2015–16 El Niño are different in different zone, China.
- Significant is inconformity between hydro-climate anomalies and floods & droughts.

GRAPHICAL ABSTRACT

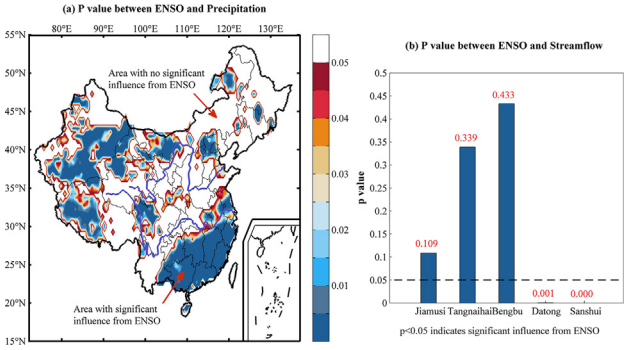

ARTICLE INFO

Article history:
Received 10 September 2017
Received in revised form 5 January 2018
Accepted 27 January 2018
Available online xxxx

Editor: Ouyang Wei

Keywords:
Hydro-climate extremes
2015–16 El Niño
Impact
China

ABSTRACT

The features of hydro-climate anomalies in China in 2015–2016 were analyzed in great detail, together with possible responses to the super 2015–16 El Niño event. The 2015–16 El Niño is characterized as a "strong" event in terms of the duration, intensity, and coverage of warming sea surface temperature (SST) in the central and east-central equatorial Pacific in comparison to the 1982–83 and 1997–98 events. The floods and droughts frequency were incidence of floods and droughts per year, respectively. The results show several significant anomalies in China: 1) About 9%–173% of precipitation variance in 2015–16 can be attributed to this El Niño; 2) There was significant inconformity between hydro-climate anomalies and the occurrence of floods and droughts; 3) Flood frequency has increased, especially over Southeast China and the Yangtze River in the summer of 2016; 4) Drought frequency has also increased, especially over Northeast China in summer of 2015, Northwest China in spring of 2016, and most parts in winter of 2015. The response of China hydro-climate anomalies to the 2015–16 El Niño was significant via El Niño and warm Indian Ocean induced circulation anomalies, which were characterized by stronger and more westward-extending western Pacific subtropical high and anomalous water vapor transport. Knowledge of the response of hydro-climate extremes to El Niño can provide valuable information to improve flood and drought forecasting in China.

1. Introduction

El Niño is a warming ocean state of the El Niño Southern Oscillation (ENSO) that develops in the central and east-central equatorial Pacific, causes large-scale anomalous atmospheric circulation patterns, and

* Corresponding author.
E-mail address: azye@bnu.edu.cn (A. Ye).

https://doi.org/10.1016/j.scitotenv.2018.01.280
0048-9697/

can temporarily disrupt weather patterns around the world through interactions called "teleconnections" (Trenberth et al., 1998). The 2015–16 El Niño was considered to be one of the three strongest events on record, comparable to the strong 1982–83 and 1997–98 events (Ren et al., 2017; WMO, 2016). The warm-pool location of 2015–16 El Niño event was more westward than other events. The period of 2015–16 El Niño event was longer than other events. Disastrous weather around the world has occurred in association with this severe El Niño event (Kogan and Guo, 2017; Zhai et al., 2016). For example, global temperature in 2015 was boosted by the strong El Niño, making 2015 the hottest year since 1900 (Zhai et al., 2016). Precipitation in most regions of Australia significantly decreased during the 2015–16 El Niño (AGBM, 2016; Chen and Guan, 2016). The drought footprint in the United States peaked at 36.9% in early April 2015, i.e., about 36.9% of the United States was under drought in early April 2015. (NCEI, 2016), while southern Great Plains experienced floods in May 2015 (Wang et al., 2015).

Meanwhile, China climate has also been influenced by the strong El Niño (Chen et al., 2016; Guo et al., 2016; Nie et al., 2016; Shao et al., 2015; Wang et al., 2015; Zhai et al., 2016). For example, significant negative anomalies of summer/2015 precipitation have occurred in North China (Zhai et al., 2016). Results found that the western Pacific subtropical high (WPSH) was a prime linkage between the ENSO-induced SST anomalies and climate anomalies in China (Wang et al., 2000; Zhai et al., 2016). In general, during the El Niño, particularly in its mature phase, strong anticyclonic circulation anomalies persisted in the northwestern Pacific through Walker circulation, which caused anomalous water vapor transport to China (Zhang, 2001; Zhai et al., 2016). Meanwhile, under El Niño conditions, Indian Ocean warming generates Kelvin waves in the equatorial Indian Ocean and triggers anomalies of lower east wind and anticyclonic circulation in the Bay of Bengal (Xie et al., 2009), which further influences weather conditions in China. Meanwhile, ENSO also influences the South Asian summer monsoon through the strength of Walker Circulation, and thus influences China climate (Wang et al., 2001).

Most previous studies focused on the effect of El Niño on climate anomalies, but the response of China hydro-climate extremes (e.g. floods and droughts) to a strong El Niño remains a challenge. No two El Niños are exactly identical (Emerton et al., 2017; WMO, 2009), whereas many studies have broadly classified them into two different types: the Eastern Pacific (EP) El Niño and Central Pacific (CP) El Niño. As investigated by previous studies, the impacts of preceding El Niño events on China climate were different (Lau and Weng, 2001; Zhang et al., 1996). Generally, the positive-negative-positive (+/−/+) anomalous precipitation pattern over East Asia appears during EP El Niño (e.g., 1982–83, 1997–98), while −/+/− rainfall pattern during CP El Niño (e.g., 1991–92, 2004–05) (Yuan and Yang, 2012; Yu and Kim, 2013). For example, dry tendency over northern China and wet tendency over the Yangtze River basin were found during the 1997–98 El Niño (Lau and Weng, 2001). However, summer rainfall during 1991–92 El Niño was below average across the Yangtze and Huai River basins (Feng et al., 2016). In fact, the 2015–16 El Niño is a mixture of the EP and CP types (Paek et al., 2017), which leads to more complex impacts on China. In this paper, we will focus on (i) hydro-climate extremes in China; and (ii) its possible response to the 2015–16 El Niño. Here, the hydro-climate extremes were quantified as floods and droughts in terms of precipitation and streamflow, respectively. This paper is structured as follows: the data, methods and hydrological model are briefly described in Section 2; in Sections 3 and 4, we present the results; in Section 5, summary and discussion are provided.

2. Data, methods, and models

2.1. Data

The monthly global sea surface temperature (SST) dataset was from the NOAA Extended Reconstructed Sea Surface Temperature version 4 (ERSSTv4, http://iridl.ldeo.columbia.edu/SOURCES/.NOAA/.NCDC/.ERSST/.version4/), which covers the period from 1980 to 2016 (August 2016 in this paper). Several climate indices, which are based on SST anomalies across a given tropical Pacific region, were used to monitor an ENSO event, including Niño 1 + 2 (0–10°S, 90°W–80°W), Niño 3 (5°N–5°S, 150°W–90°W), Niño 4 (5°N–5°S, 160°E–150°W) and Niño 3.4 (5°N–5°S, 170°W–120°W). The Niño 3.4 index, which can more correctly identify the ENSO phases, comparing with other indexes (Hanley et al., 2003), was mainly used because it is the common index for identifying El Niño. In addition, the Niño 3.4 region has arguably the best teleconnections to seasonal weather and is widely used as a sampling area for SSTAs (Barnston, 2015; Null, 2015), as well as its teleconnections to China climate (Li et al., 2011; Ouyang et al., 2014; Zhai et al., 2016). The Niño 3.4 index was provided by NOAA Climate Prediction Center (http://www.cpc.ncep.noaa.gov/data/indices/ersst4.nino.mth.81-10.ascii).

The gridded daily precipitation and surface temperature observations covering 1980–2016 (August 2016 in this paper) at a 0.5-degree resolution were obtained from the National Meteorological Information Center, CMA (http://data.cma.cn/data/index/00f8a0e6c590ac15.html), which have been interpolated from 2472 meteorological stations using the Thin Plate Spline (TPS) method (Hutchinson, 1998a, 1998b). The maximum, minimum and mean temperatures were used to calculate the potential evapotranspiration for the hydrological model using Hargreaves & Samani method (Arnold et al., 1997; Hargreaves et al., 2003; Pereira et al., 1999; Raziei and Pereira, 2013). The daily streamflow datasets (1980–2016) included two sources: historical observations from the hydrology bureau (Table 1: calibration and validation periods) and simulations using a distributed time-variant gain model (DTVGM) hydrological model (see Section 2.4), considering unavailable real-time observations. These stations were chosen because they are control stations located on the main channel of five main rivers in China and had long and relatively continuous time series for calibration. In this study, the Precipitation Anomaly Percentage (PAP) and Streamflow Anomaly Percentage (SAP) were used as indicators for precipitation and streamflow anomalies, respectively. Here, a climatological base period of 1981–2010 is used for the calculation of PAP and SAP (Wright, 2014). Streamflow is the flow of water in rivers. The streamflow was an index to evaluate flood in this paper, considering the nonlinearity between precipitation and flood (Emerton et al., 2017). Hydro-climate anomalies can change streamflow, but the flood may not occur until the streamflow exceeded the threshold.

The monthly PAP and SAP are calculated as:

$$PAP_{i,j} = \frac{P_{i,j} - \overline{P}_i}{\overline{P}_i} \quad (1)$$

$$SAP_{i,j} = \frac{S_{i,j} - \overline{S}_i}{\overline{S}_i} \quad (2)$$

where $P_{i,j}$ is precipitation at i^{th} month and j^{th} year, $S_{i,j}$ is streamflow at i^{th} month and j^{th} year, $\overline{P}_i$ and $\overline{S}_i$ are the average precipitation and streamflow at i^{th} month, respectively.

Here, a flood is identified using the following criteria.

Table 1
Station attributes.

Name	Basins	Longitude	Latitude	Calibration	Validation
Jiamusi	Songliao	130.37	46.81	1980–1991	1992–2002
Tangnaihai	Yellow river	100.15	34.50	1980–1993	1994–2007
Bengbu	Huai river	117.38	32.95	1980–1993	1994–2007
Datong	Yangtze river	117.61	30.78	1980–1993	1994–2007
Sanshui	Pearl river	112.5	23.1	2001–2002	2003

1) Heavy precipitation accumulated over a 7-day period (or daily mean Streamflow), which exceeded the threshold of the 95th percentile of the 7-day data over the entire time period (Fig. A.1; Ding et al., 2009).
2) The 7-day PAP (or daily SAP) exceeded 80%.
3) The precipitation accumulation for 7 days exceeded 100 mm (Ding et al., 2009).

Similarly, a dry spell/drought is defined as:

1) Low precipitation accumulation for 20 days (or daily mean Streamflow) below the threshold of the 5% percentile of 20-day data over the entire time period.
2) The 20-day PAP (or daily SAP) was less than −80%.

The n1-day accumulated PAP is calculated as:

$$PAP_{(d,j,n1)} = \frac{\sum_{i1=1}^{n1} P_{(d-i1+1,j)} - \frac{1}{n2}\sum_{j=1}^{n2}\sum_{i1=1}^{n1} P_{(d-i1+1,j)}}{\frac{1}{n2}\sum_{j=1}^{n2}\sum_{i1=1}^{n1} P_{(d-i1+1,j)}} \quad (3)$$

where, $\sum_{i1=1}^{n1} P_{(d-i1+1,j)}$ is precipitation accumulation for the past *n1* days; *n2* refers to 30 years (1981–2010).

The daily SAP is calculated as:

$$SAP_{(d,i,j)} = \frac{S_{(d,i,j)} - \overline{S}_{(d,i)}}{\overline{S}_{(d,i)}} \quad (4)$$

where $S_{(d,i,j)}$ is streamflow at d^{th} day, i^{th} month and j^{th} year; $\overline{S}_{(d,i)}$ are the average streamflow at d^{th} day and i^{th} month.

2.2. The autoregressive (AR) model

In statistics, an AR model (Lin et al., 2013; Zhao and Shen, 2011) is a type of random process, which is often used to predict variable depended linearly on its own previous values and a stochastic term. The AR model can be written as:

$$y_t = \mu + \varphi_1(y_{t-1} - \mu) + \varphi_2(y_{t-2} - \mu) + \cdots + \varphi_p\left(y_{t\text{-}p} - \mu\right) + \varepsilon_t \quad (5)$$

where, μ is a constant, ε_t is white noise. $\varphi_1, \varphi_2, \cdots, \varphi_p$ are the parameters of the model. p is the order, which was obtained by Akaike Information Criterion (AIC; Akaike, 1969) as Eq. 6, with the smallest AIC.

$$AIC(p) = n\ln(\sigma_\varepsilon^2) + 2p \quad (6)$$

where, n is the time span, σ_ε^2 of the residual (ε_t).

Here, given the 2015–16 El Niño as an abrupt event, the quantitative estimations was obtained as Eq. 7.

$$Q_t = \frac{P_t - y_t}{y_t} \quad (7)$$

where, P_t is the observed precipitation.

2.3. Granger causality test (GCT)

In this paper, the Granger causality test (GCT; Granger, 1969) was used to investigate the effect of the El Niño on precipitation and streamflow anomalies. The GCT was first proposed for a potential causality relationship between two variables in econometrics and has been widely applied to the fields of climate systems (Attanasio, 2012; Jiang et al., 2015; Sun et al., 2016). Unlike other conventional statistical methods, the GCT can be used to detect the causal relationships in terms of predictability (Jiang et al., 2015). Here, the test process of GCT is described as follows:

1) Before applying the GCT, we must test the stability of the variables using the augmented Dickey-Fuller (ADF) test (Dickey and Fuller, 1981). The ADF test is specified as:

$$\Delta\omega_t = q_0 + q_1 t + \varphi\omega_{t-1} + \sum_{j=1}^{p}\Delta\omega_{t-j+1} + \varepsilon_t \quad (8)$$

where, ε_t is white noise, q_0 is a constant. p is lag order of the AR process (see Section 2.2). The null hypothesis is that the time series is nontrend stationary. The ADF statistic is:

$$ADF_t = \frac{\hat{\varphi}}{se(\hat{\varphi})} \quad (9)$$

where, $\hat{\varphi}$ is the ordinary least squares (OLS) estimate of φ, and $se(\hat{\varphi})$ is the standard error of $\hat{\varphi}$. If the test statistic is less than the critical value, then the null hypothesis is rejected. We confirmed that the time series of the Niño 3.4 index, PAP and SAP were stationary.

2) Then, the GCT was established as the unrestricted model (Eq. 10), which specifies the full set of climate and precipitation (streamflow) anomaly information;

$$X_n = \sum_{j=1}^{m_1}\alpha_j X_{n-j} + \sum_{i=1}^{m_2}\beta_i Y_{n-i} + \varepsilon_n \quad (10)$$

and the restricted model (Eq. 11), which only uses previous climate precipitation (streamflow) anomaly information.

$$X_n = \sum_{j=1}^{m_1} r_j X_{n-j} + u \quad (11)$$

where X is the PAP or SAP; Y is the Niño 3.4 index; α, β and r are the coefficients of models, which are estimated by OLS (Attanasio, 2012); ε and u are the errors; n is the time span; and m_1 and m_2 are the optimal time lags, which were obtained using the Bayesian information criterion (BIC; Schwarz, 1978), with the smallest BIC.

$$BIC(t) = n \times \ln\left(\frac{Rss_x}{n}\right) + (s+1) \times \ln(n) \quad (12)$$

$$Rss_x = \sum_{t=1}^{T}\left(X_t + \hat{X}_t\right)^2 \quad (13)$$

where t is the time lag (1–12 months in this paper) for X; Rss_x is the residual sum of squares for Eq. (10). The optimal lagged month (m_2) for Y is determined similarly to m_1.

3) Then, we simply use an F test with the null hypothesis that Y cannot Granger-cause X to examine the statistical significance between restricted estimates of X (Rss_x) and Y (Rss_y):

$$F = \frac{(Rss_x + Rss_y/m_2)}{Rss_y/(n - m_1 - m_2 - 1)} \quad (14)$$

If the p values obtained from the F test are lower than a significance level (0.05 in this paper), the null hypothesis can be rejected, i.e., Y can Granger-cause X.

2.4. Hydrological model

In this paper, the distributed time-variant gain model (DTVGM) hydrological model (Xia et al., 2005; Ye et al., 2010), which has been used

to simulate China hydrological conditions (Mao et al., 2016), was applied to simulate the unavailable streamflow in China.

Five hydrological stations, spread throughout five different drainage basins in China, were used in this paper. The locations and information of the five stations are shown in Fig. 1 and Table 1. The DTVGM was calibrated at the five stations and used to simulate the unavailable streamflow. The DTVGM was also calibrated using default parameters, which have been calibrated in other similar basin (Xia et al., 2003; Xia et al., 2005), to simulate streamflow in western China, because of undocumented streamflow data of international rivers. The major parameters are the runoff coefficient (g_1, $0 < g_1 < 1$), soil moisture parameter (g_2, $g_2 > 0$), sub-surface runoff coefficient (Kr, $0 < Kr < 1$), groundwater runoff coefficient (Kg, $0 < Kg < 1$), infiltration rate (fc, 0–30 mm/h) and Manning roughness coefficient (n, $0.001 < n < 0.15$; Huggins and Monke, 1966). The calibration and validation results are shown in Table 2. The Nash-Sutcliffe efficiency (NSE) during the calibration and validation periods were >0.64 and even larger than 0.8 for the Tangnaihai and Datong stations. The correlation coefficients R during the calibration and validation periods were larger than 0.8, and the balance coefficients B were nearly 1. Fig. 2 shows the streamflow curves of five stations during the calibration and validation periods. The simulated streamflow matched the observed streamflow well during both the calibration and validation periods, which indicates that the simulated streamflow from running the DTVGM model can be used as the absent "observations" to analyze the hydrologic anomalies and extremes in China as well as its relationship with the El Niño.

Table 2
Model performance during the calibration and validation periods*.

	Indices	Jiamusi	Tangnaihai	Bengbu	Datong	Sanshui
Calibration period	R	0.88	0.93	0.87	0.95	0.9
	NSE	0.71	0.84	0.68	0.88	0.81
	B	0.913	0.911	0.982	0.95	0.919
Validation period	R	0.88	0.91	0.88	0.94	0.87
	NSE	0.65	0.79	0.73	0.85	0.64
	B	1.034	1.093	1.134	0.926	0.8

* R: correlation coefficient; NSE: Nash-Sutcliffe efficiency; B: balance coefficient.

3. The 2015–16 floods and droughts in China

Fig. 3a–f show the distribution of the seasonal PAP from spring 2015 to summer 2016. The seasonal PAP represents the variations of the precipitation amount. The mean precipitation over China in spring 2015 was 145 mm, which approached the climatological normal but with strong intra-seasonal variations (Shao et al., 2015). Fig. 3a clearly shows that the precipitation in western Inner Mongolia, North China, northeast China, parts of Northwest China, western Qinghai, and eastern Tibet increased by 25–50%; the partial areas were >50%. However, precipitation decreased by 25–50% in western Xinjiang and >50% in the south of southwestern China. In summer 2015, precipitation was below normal in most parts of China (Fig. 3b), which included the northern regions of China (i.e., North China, Yellow-Huai valleys, eastern part of Northwest China, Inner Mongolia, and Northeast China), western China and Tibet (Wang et al., 2015). The average rainfall over China in autumn 2015 was 151 mm, which was wetter than average (Nie et al., 2016). Precipitation increased (>50%) in Northwestern China, central-western Inner Mongolia, northern parts of North China, eastern Yellow-Huai valleys and most of South China, whereas rainfall decreased in Tibet, western-southwestern Xinjiang, northeastern Inner Mongolia, eastern parts of Northeastern China, southern Henan, southern Guangdong and western Hainan (Fig. 3c). The mean rainfall over China in winter 2015 was 62.3 mm, with an increase of 52.7%. Positive precipitation anomalies occurred in central Northeastern China, western Inner Mongolia, southern Tibet and South China, and negative anomalies occurred in the Yellow-Huai River valley, Yangtze-Huai River area and western Xinjiang (Fig. 3d). The mean precipitation over China in spring 2016 was 174.9 mm, which was 20% higher than the climatological average. The precipitation was more than the average in the eastern parts of Northeast China, western Inner Mongolia, central-eastern Tibet, Yangtze-Huai River area and central-eastern South

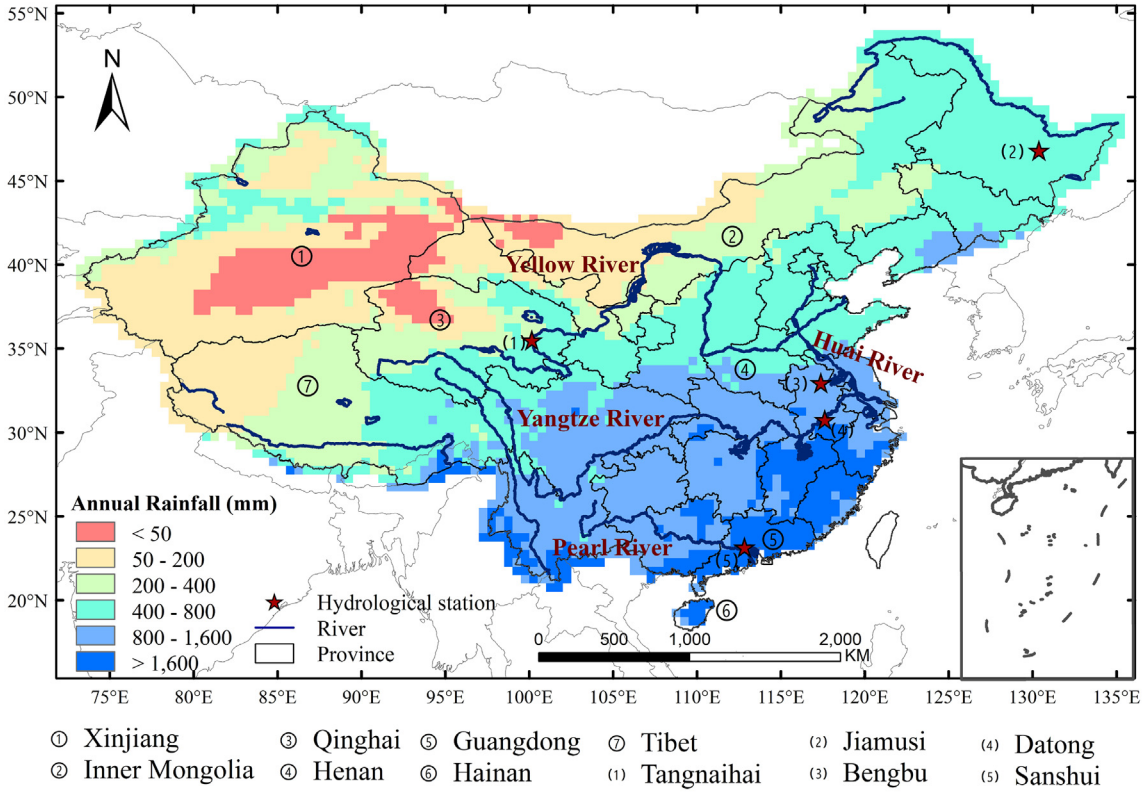

Fig. 1. Locations of the hydrological stations in this paper.

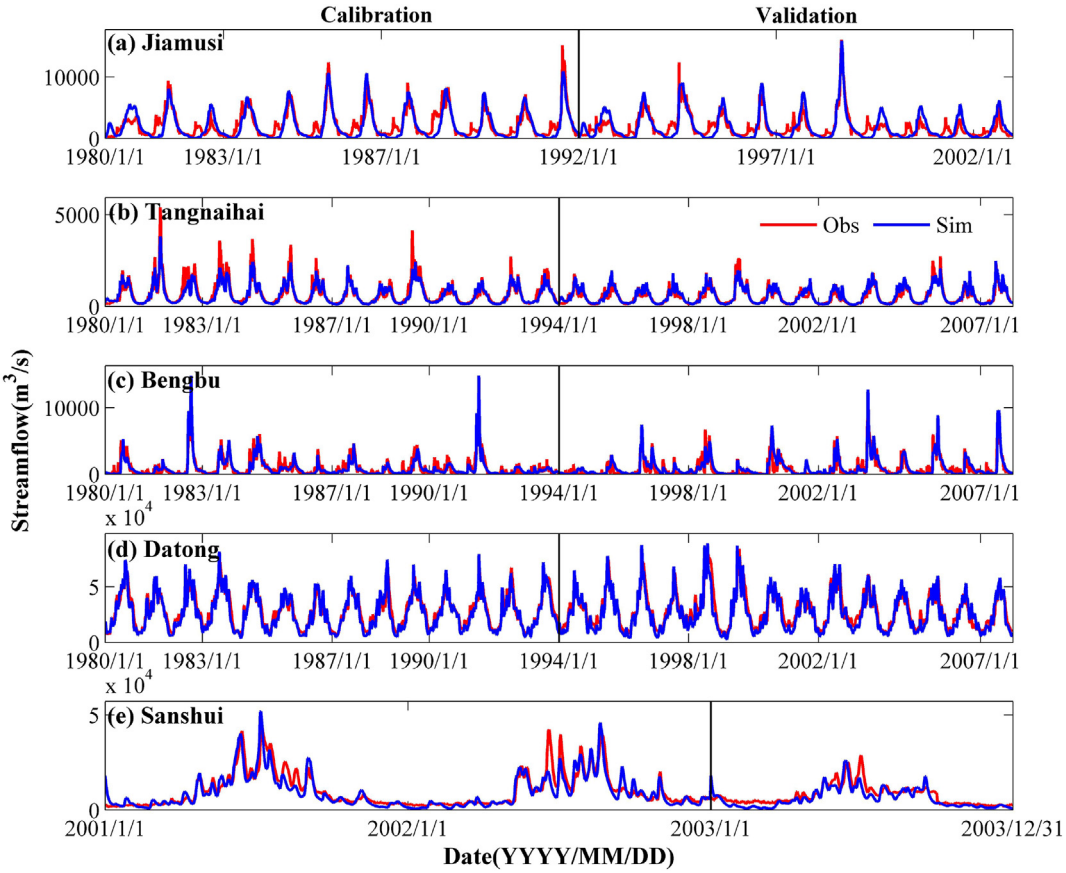

Fig. 2. Streamflow curve of the five stations during the calibration period (left panel) and validation period (right panel).

China (Fig. 3e). By contrast, less precipitation occurred in western Xinjiang, northwestern Tibet, central-eastern Inner Mongolia, North China and the Yellow-Huai River valley (Fig. 3e). During summer in the El Niño decaying year, the precipitation increased by over 50% in the Yangtze-Huai River areas, southern Tibet, western Inner Mongolia, and eastern parts of North China, but decreased in northeastern Inner Mongolia, Yellow-Huai valleys, and the south coastal areas (Fig. 3f).

Increasing or decreasing precipitation anomalies do not necessarily imply the occurrence of floods or dry spells. Fig. 4a–f show the differences in flood frequency between the 2015–16 El Niño and normal phases (excluding El Niño and La Niña years). Fig. 5a–f show the dry spells frequency anomalies. The frequency of floods and dry spells during the 2015–16 El Niño event increased in comparison to the normal conditions, which indicates that more extreme events occurred in China during 2015–16 (NCCCMA, 2016). The covering areas of climate extremes were highest in April–July during 2015–16 El Niño. Fig. 4 shows that the flood frequency did not obviously increase and that there was a significant increase in southeastern China. Despite negative seasonal precipitation anomalies in summer 2015, the flood frequency increased instead, particularly in eastern coastal China. However, positive seasonal PAP did not significantly increase the flood frequency in southeastern China during autumn-winter 2015 and Inner Mongolia during autumn 2015. Floods significantly increased in southeastern China in spring 2015 and in the middle and lower reaches of the Yangtze River in summer 2016 with the increased amount of seasonal precipitation. As shown in Figs. 3 and 5, the lack of precipitation caused significantly increased dry spells in Liaoning province in summer 2015, but there was no obvious increase in other regions. More dry spells also occurred in most of China in winter 2015 and Northwest China in spring 2016 than in normal phases.

Fig. 6a–e show the seasonal streamflow anomaly percentage (SAP) during the El Niño events. In the Songliao River basin, positive streamflow anomalies occurred from winter 2015-summer 2016 and negative anomalies occurred in spring 2015. Larger streamflows occurred in the upstream of the Yellow River basin in spring 2016. The anomalies in spring 2015, autumn 2015 and spring 2016 were negative and relatively small in the Huai River basin. The Yangtze River basin experienced positive streamflow anomalies in winter 2015 and summer 2016, and so did the Pearl River basin in winter 2015. Fig. 7a–e show the difference in the frequency of floods and droughts (defined by streamflow) between the 2015–16 El Niño and normal phases (excluding El Niño and La Niña years). There were increased floods in the Huai River basin in winter 2015. More floods occurred in the Yangtze River basin in summer 2016, which was similar to the precipitation anomalies. More droughts also occurred in the Pearl River basin in spring 2016.

4. Feature of the 2015–16 El Niño and its impact on China

Fig. 8a–c show the progression of the three Niño indices (Niño 3, Niño 4 and Niño 3.4 index) across the equatorial Pacific for three El Niño events in comparison with the average of all El Niño events and the other El Niño events (remove the three strong events) since 1980. The 1982–83, 1997–98, and 2015–16 El Niño events were the three strongest events on record, with nearly identical peak tropical SST anomalies (Niño 3.4 index) of 2.4 °C, which were apparently higher than those of other El Niño events as well as that of the mean El Niño. However, the SST anomalies in the Niño 4 (Niño 3) regions during the 2015–16 El Niño were higher (less) than those during the 1982–83 and 1997–98 events (Fig. 8a–b). Those indicated that the location of SST extreme during the 2015–16 El Niño was to west compared with that during other events (Lim et al., 2017; Paek et al., 2017). Fig. 8d–f compare the temporal evolution of SST anomalies over the equatorial Pacific during the three strong El Niño events. The 1982–83 and 1997–98 El Niño events were characterized by shorter durations and

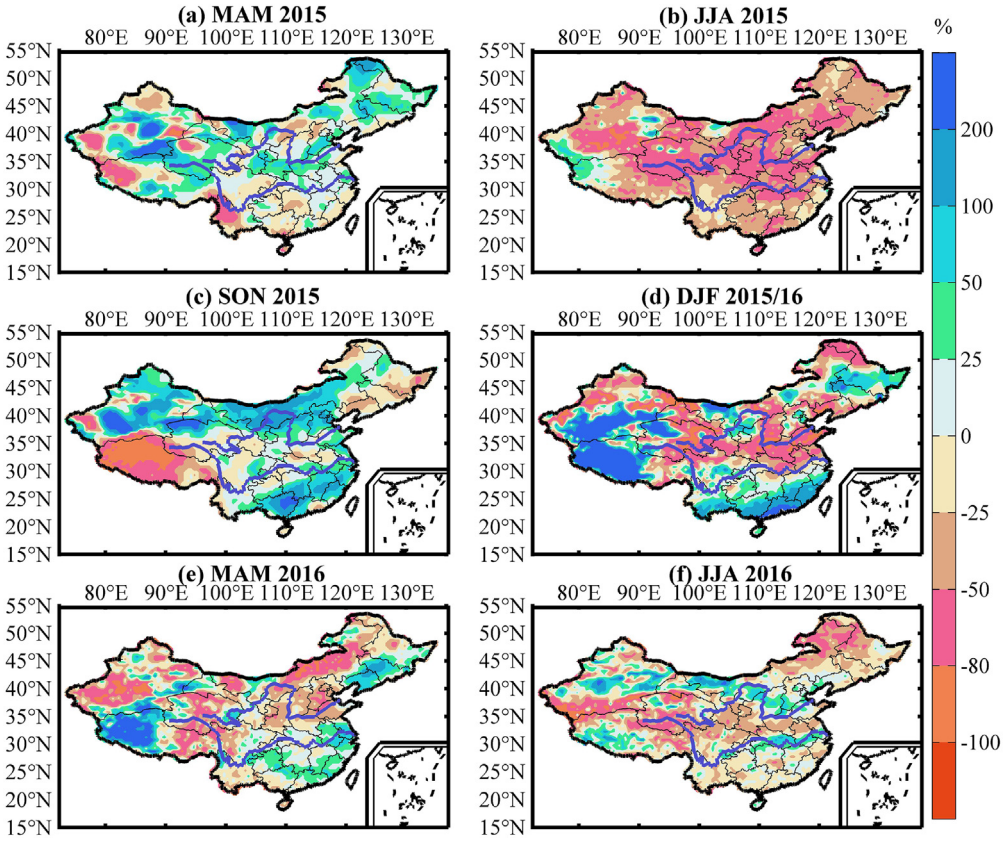

Fig. 3. Spatial distributions of the precipitation anomaly percentage (PAP, %) in China: (a) spring 2015, (b) summer 2015, (c) autumn 2015, (d) winter 2015/16, (e) spring 2016, and (d) summer 2016.

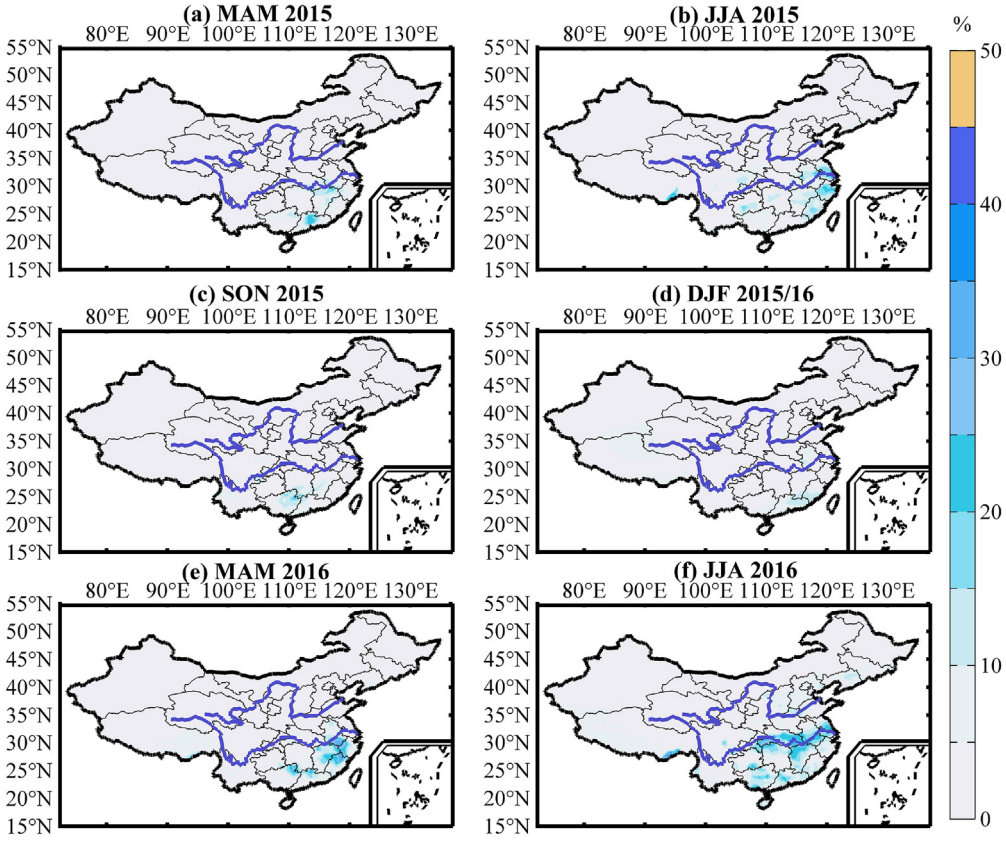

Fig. 4. Spatial distributions of the anomalies of the occurrence frequency (%) of floods in China during (a) spring 2015, (b) summer 2015, (c) autumn 2015, (d) winter 2015/16, (e) spring 2016, and (d) summer 2016, with respect to the corresponding season in normal years.

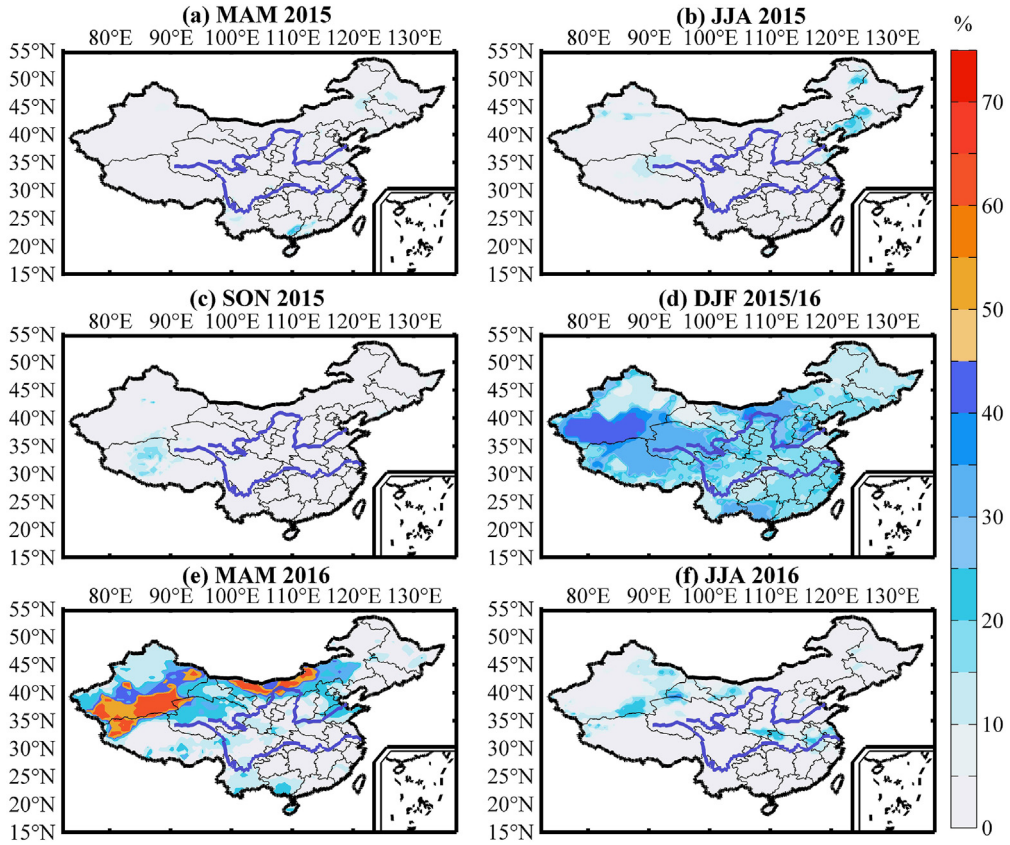

Fig. 5. Spatial distributions of the anomalies of the occurrence frequency (%) of dry spells in China during (a) spring 2015, (b) summer 2015, (c) autumn 2015, (d) winter 2015/16, (e) spring 2016, and (d) summer 2016, with respect to the corresponding season in normal years.

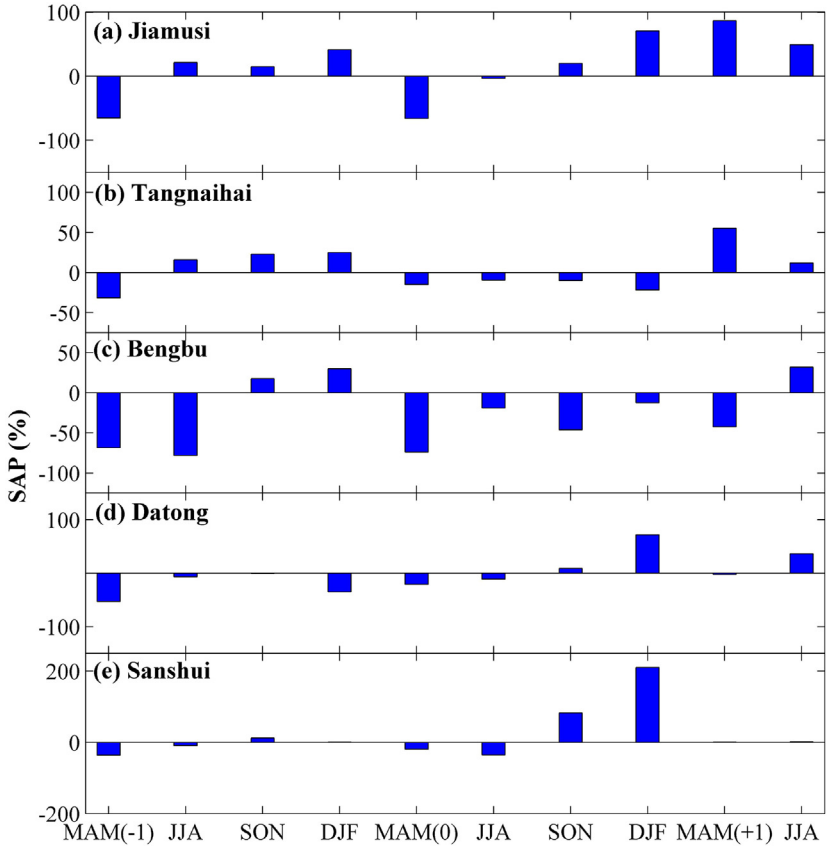

Fig. 6. Seasonal mean streamflow anomaly percentage (SAP, %) for the 2015–16 El Niño events at (a) Jiamusi, (b) Tangnaihai, (c) Bengbu, (d) Datong, (e) Sanshui, where −1, 0 and 1 in the brackets refer to the year prior to the onset of El Niño, El Niño developing and decaying years, respectively.

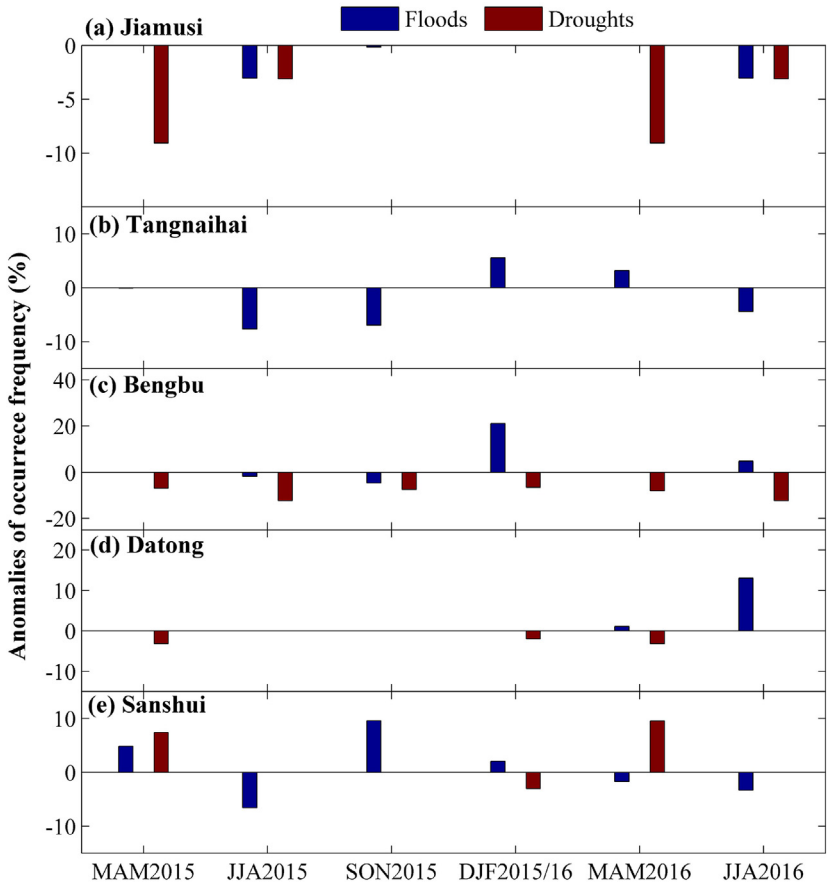

Fig. 7. Anomalies of the occurrence frequency (%) of floods and droughts from spring 2015 to summer 2016 with respect to the normal years in (a) Jiamusi, (b) Tangnaihai, (c) Bengbu, (d) Datong, (e) Sanshui (the solid blue columns represent the floods; the red columns represent the droughts). (For interpretation of the references to color in this figure legend, the reader is referred to the web version of this article.)

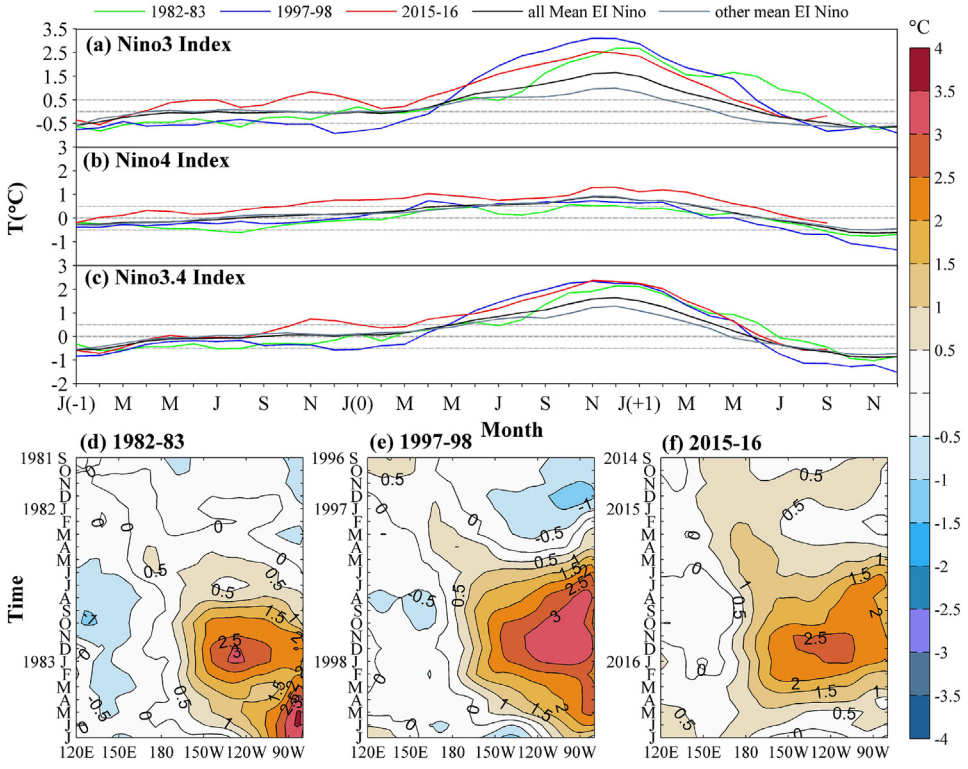

Fig. 8. Three-year progression of the (a) Niño 3 index, (b) Niño 4 index, (c) Niño 3.4 index for three super El Niño events (1982–83, 1997–98, 2015–16), as well as the average of all El Niño events (black line) and the other El Niño events (grey line) since 1980, where −1, 0 and 1 in the brackets refer to the year prior to the onset of El Niño, El Niño developing and decaying years, respectively. Temporal evolution of the SST (°C) anomalies of (d) 1982–83, (e) 1997–98, and (f) 2015–16 El Niño events over the equatorial Pacific, which were averaged from 5°S to 5°N.

smaller ranges, but high peak anomalies (Fig. 8b–c). However, in 2015–16, a significantly longer duration up to >20 months was observed with persistent positive SST anomalies (>0.5) from autumn 2014 through spring 2016. Fig. 9a–f further display the development of the 2015–16 El Niño event, via global SST anomalies with Niño 3.4 regions marked in rectangular boxes at the specified month. From May 2014, anomalous SST warming persisted in the equatorial central and eastern Pacific, whereas the El Niño developed into a strong event after November 2014 and reached its peak in November–December 2015 (Figs. 8a, d and 9d). Meanwhile, large-scale positive SST anomalies covered the entire equatorial central and eastern Pacific with SST anomalies larger than 0.5 °C in most of the ocean area (Figs. 8c and 9b–e). The 2015–16 El Niño exceeded the 1982–83 and 1997–98 events in terms of the index of duration, intensity, accumulated SST anomalies, and months when the SST anomalies consecutively exceeded 2 °C.

Previous studies have stated that precipitation anomalies in China can be partially explained by atmospheric circulation anomalies associated with the ENSO (Feng et al., 2016; Jin et al., 2016; Li et al., 2011; Li and Ma, 2012; Wu and Wang, 2002; Wu et al., 2003; Yuan and Yang, 2012; Zhang et al., 1999). This paper further confirms the causal relationships between the precipitation (streamflow) anomalies and ENSO for mainland China in 1980–2016 (Fig. 10). The GCT results reveal a causal relationship between the PAP and Niño 3.4 in Southeast China and parts of Northwest China (Fig. 10a), which was approved by statistically significant testing with smaller p values than 0.05 (at the 95% confidence level). The relationship also varies with seasons (Fig. A.2). In general, the optimal lag time was 1–2 months, which shows that the precipitation response to the ENSO was not synchronous and exhibited 1–2 months of lag time. This finding provides critical information for precipitation predictions using the ENSO signals from the previous 1–2 months as potential predictors. In addition, the GCT results confirm that the El Niño significantly affected the Yangtze River and Pearl River basins, but an insignificant effect was found in the Yellow-Huai River and Songliao River basins (Fig. 10b). In general, based on the hydrologic lags, the effect of an El Niño can be delayed with an optimal lagged time of 1–3 months, which surpassed that of precipitation.

The hydro-climate anomalies in China could be related to the 2015–16 El Niño. Quantitative estimates using AR model reveal that on the average over all China, approximately 9%–173% of precipitation variance in 2015–16 can be attributed to the 2015–16 El Niño (Table 3). Many researchers also have stated that the 2015–16 El Niño and El Niño-induced Indian Ocean warming together resulted in precipitation anomalies in China (Nie et al., 2016; Shao et al., 2015). During the 2015–16 El Niño, positive SST anomalies were observed over the equatorial central-eastern Pacific and Indian Ocean (Fig. 9b–e). This SST configuration induced anomalous ascent over the equatorial central and eastern Pacific and Indian Ocean, and thus altered Walker circulation (Chen et al., 2016; Guo et al., 2016; Nie et al., 2016; Shao et al., 2015; Wang et al., 2015; Wu et al., 2016; Xiao et al., 2016; Yuan et al., 2016; Yuan et al., 2017; Zhai et al., 2016). Consequently, the resultant descent anomalies were appeared and suppressed the convection activities over the northwestern Pacific. This circulation anomalies excited lower-tropospheric anticyclonic anomalies over the northwestern Pacific and leaded to intensification and southwestward extension of the western Pacific subtropical high. Meanwhile, the anomalous warming Indian Ocean also exacerbated the lower-tropospheric anticyclonic anomalies through Kelvin wave. In fact, the location and intensity of the western Pacific subtropical high, which can influence monsoon and water vapor transport around China and further influence China climate, vary with seasons. In March–April 2015, the westward shifting and intensified western Pacific subtropical high resulted in negative anomalies of water vapor transport from southwestern monsoon and

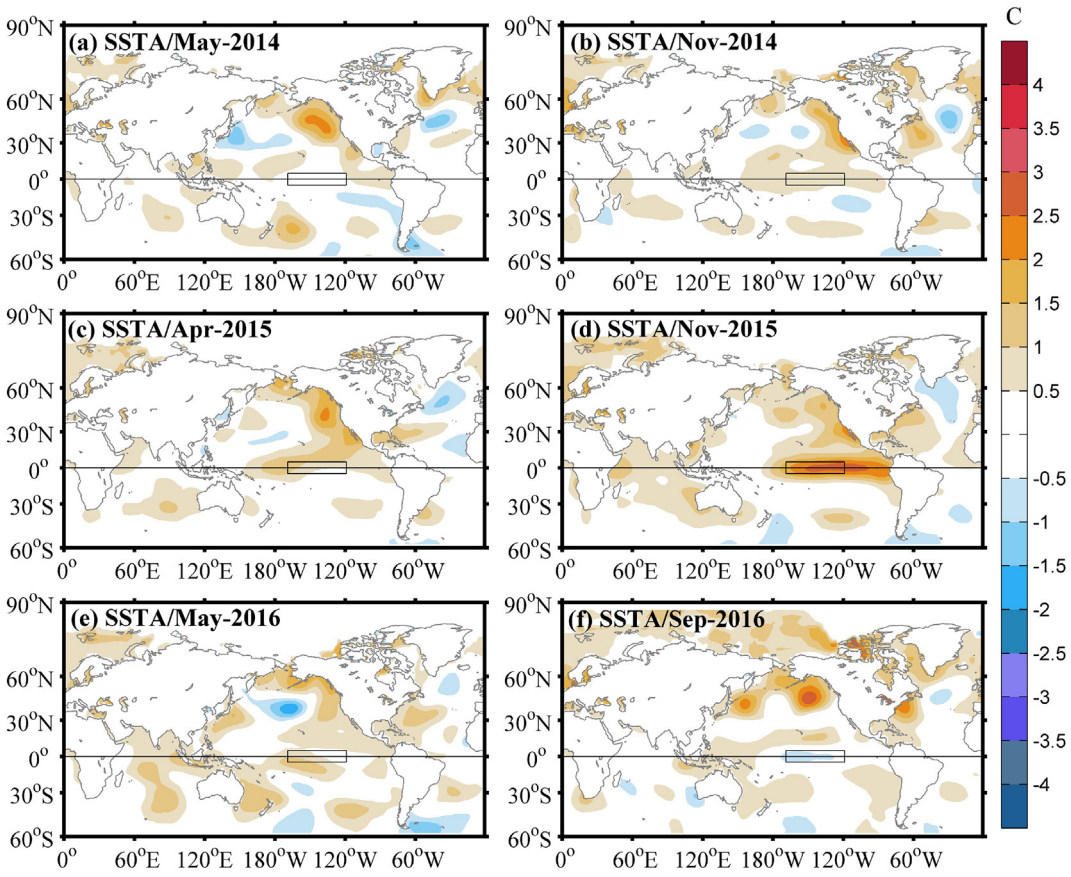

Fig. 9. Spatial distributions of global SST anomalies in (a) May 2014, (b) November 2014, (c) April 2015, (d) November 2015, (e) May 2016, and (f) September 2016 during the 2015–16 El Niño events. The rectangular boxes mark the Niño 3.4 regions.

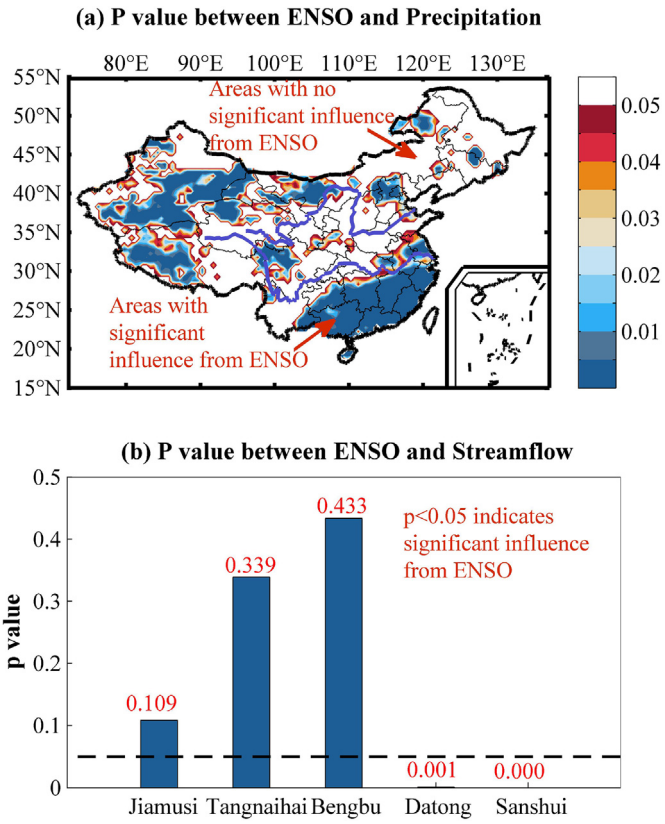

Fig. 10. The Granger causality test p values, (a) Spatial distribution of the Granger causality test p values for the PAP and the Niño 3.4 index during 1980–2016. The color-shaded areas represent the regions with statistically significant results ($p < 0.05$). (b) Granger causality test p values for the SAP and the Niño 3.4 index at five hydrologic stations during 1980–2016. The p values below 0.05 (black dash line) indicate the station is significantly affected by ENSO.

ambient subtropical high to South China (Shao et al., 2015; Wu et al., 2016). In May 2015, the water vapor transport to China via Indian Ocean was formed, leading to positive precipitation anomalies in South China (Shao et al., 2015). In summer 2015, the western Pacific subtropical high was south, west and stronger than normal, preventing the water vapor transport to North China (Wang et al., 2015). Southwestern China was dominated by northerly and westerly flow, bringing on no obvious water vapor convergence and less rainfall there (Wang et al., 2015). Meanwhile, there was a powerful high pressure system over Tibetan Plateau, thereby resulting in less precipitation. The lower-tropospheric anticyclonic anomalies further enhanced in autumn 2015 with the development of the El Niño (Nie et al., 2016) and peaked in winter 2015 (Zhai et al., 2016), leading to the strengthened and westward western Pacific subtropical high. Consequently, the anomalously strong southerly water vapor transport from the South China sea and western Pacific to South China appeared along western side of western Pacific subtropical high, causing the wetter autumn and winter there (Nie et al., 2016; Yuan et al., 2016; Zhai et al., 2016). Meanwhile, strong cold air processes, caused by larger amplitude ridges and troughs in mid-latitude areas, together with water vapor transport from South China sea and East China sea brought about more rainfall over North China in autumn 2015 (Nie et al., 2016). In spring and summer 2016, although the El Niño was decaying, the lower-tropospheric anticyclonic anomalies was maintained, caused by persistent warm SST in western Pacific warm pool and Indian Ocean (Chen et al., 2016; Yuan et al., 2016). Subsequently, the western Pacific subtropical high was west and stronger than normal, leading to more rainfall over South China in spring 2016 and Yangtze River basin in summer 2016 (Chen et al., 2016; Guo et al., 2016; Xiao et al., 2016; Yuan et al., 2016; Yuan et al., 2017).

Table 3
Quantitative estimates using AR model of precipitation in China effected by the 2015–16 El Niño.

2015 Spring	2015 Summer	2015 Autumn	2015 Winter	2016 Spring	2016 Summer
−9.1%	−37.7%	172.8%	34.4%	−14.5%	−12.1%

5. Summary and discussion

The precipitation and streamflow anomalies features in 2015–2016 have been analyzed in great detail in this paper. Positive hydro-climate anomalies generally occurred in Inner Mongolia in autumn 2015, southeast China in winter 2015, and the middle and lower reaches the Yangtze River in late spring-summer 2016; while negative anomalies occurred in northeast China from summer-winter 2015, north China in summer 2015 and winter/2015–spring/2016, and eastern Inner Mongolia in summer 2015 and winter/2015–summer/2016. However, seasonal hydro-climate anomalies only represent anomalies of the amount of precipitation or streamflow and do not necessarily cause the occurrence of floods and droughts. Here, we quantify the occurrence of floods and droughts and analyzed their frequency variations. Results found that the frequencies of meteorological floods and droughts have increased in 2015–2016. The decreased amount of precipitation and increased flood frequency in eastern China in the summer of the developing year may indicate more concentrated precipitation and severe extreme flood events. Increased precipitation and more frequent floods also occurred in the middle and lower reaches of the Yangtze River in the summer of the decaying year. This finding was also demonstrated in the streamflow results. However, there were reduction of hydrological floods and droughts, which may be attributed to the initial conditions and human activities.

Previous researches have stated that the ENSO-like SST anomalies in the tropical Pacific have significant effect on China climate, with 1–3 months lag. Considering the 2015–16 El Niño was the one of strongest event since 1980, the hydro-climate anomalies in China could largely explained by the circulation anomalies induced by this El Niño. The 2015–16 El Niño persisted for >20 months, which developed in autumn 2014 and peaked in November–December 2015 and returned to ENSO-neutral levels by May 2016. The El Niño-like SST configuration together with anomalous warm Indian Ocean induced lower-troposphere anticyclonic anomaly over the western North Pacific. Consequently, the western Pacific subtropical high intensified and extended southward and westward, enhancing or preventing water vapor transport to China during different seasons. To conclude, the intensity and location of western Pacific subtropical high and water vapor transport varied with seasons, thereby caused the occurrence of floods and droughts over different regions in China. Meanwhile, quantitative estimates also reveal that on the average over all China, approximately 9%–173% of precipitation variance in 2015–16 can be attributed to the 2015–16 El Niño.

However, the effect of El Niño on the hydro-climate in China is complex, and often accompanied by other climate factors (e.g., the Eurasia-Pacific teleconnection pattern, Pacific decade oscillation, Indian Ocean Capacitor), which also can cause regional and seasonal hydro-climate anomalies in China (Feng et al., 2014; Wang and Zhang, 2015; Xie et al., 2009). In addition, hydro-climate processes are nonlinear with many other influence factors except for teleconnection (Ouyang et al., 2015; Ouyang and Gao, 2017; Xu et al., 2014). Therefore, the impact mechanism of the hydro-climate in China requires additional study, which will be valuable to improve extreme-hydro-climate-event forecasting and water resource management in China. In addition, real-time hydrological observation datasets are expected to verify the robustness of the results.

Acknowledgements

This work was supported by the Natural Science Foundation of China [No. 41475093]; the Intergovernmental Key International S&T Innovation Cooperation Program [No. 2016YFE0102400]; and the State Key Laboratory of Earth Surface Processes and Resource Ecology Open Research Program (NO. 2017-KF-17). We would like to thank China Meteorological Administration (http://data.cma.cn) for making precipitation and temperature information available and hydrology bureau for providing streamflow data.

Appendix A. Supplementary data

Supplementary data to this article can be found online at https://doi.org/10.1016/j.scitotenv.2018.01.280.

References

Akaike, H., 1969. Fitting autoregressive models for prediction. Ann. Math. Stat. 21 (1), 243–247.
Arnold, J.G., Williams, J.R., Srinivasan, R., 1997. Model Theory of SWAT. USDA. Agricultural Research Service Grassland. Soil and Water Research Laboratory, USA.
Attanasio, A., 2012. Testing for linear granger causality from natural/anthropogenic forcings to global temperature anomalies. Theor. Appl. Climatol. 110:281–289. https://doi.org/10.1007/s00704-012-0634-x.
Australian Government Bureau of Meteorology (AGB-M), 2016. El Niño - detailed Australian analysis. http://www.bom.gov.au/climate/enso/enlist/.
Barnston, A., 2015. Why are there so many ENSO indexes, instead of just one? https://www.climate.gov/news-features/blogs/enso/why-are-there-so-many-enso-indexes-instead-just-one
Chen, W., Guan, Z., 2016. Impacts of the super El Nino event in 2015/16 on Australian summer monsoon circulation and precipitation anomalies. Trans. Atmos. Sci. 39 (6), 801–812 (in Chinese).
Chen, J., Wen, Z., Wang, X., 2016. Analysis of winter and spring precipitation over Southern China during 2015/2016 extreme El Niño. Trans. Atmos. Sci. 39 (6), 813–826 (in Chinese).
Dickey, D.A., Fuller, W.A., 1981. Likelihood ratio statistics for autoregressive time series with a unit root. Econometrica 49 (4):1057–1072. https://doi.org/10.2307/1912517.
Ding, Y., Zhang, J., et al., 2009. Rainstorm and Flood. Meteorological Press, Beijing (in Chinese).
Emerton, R., Cloke, H.L., Stephens, E.M., Zsoter, E., Woolnough, S.J., Pappenberger, F., 2017. Complex picture for likelihood of ENSO-driven flood hazard. Nat. Commun. https://doi.org/10.1038/ncomms14796.
Feng, J., Wang, L., Chen, W., 2014. How does the east Asian summer monsoon behave in the decaying phase of El Niño during different PDO phases? J. Clim. 27, 2682–2698.
Feng, J., Li, J., Zhang, F., et al., 2016. Contrasting impacts of developing phases of two types of El Niño on southern China rainfall. J. Meteorol. Soc. Jpn. 94 (4):359–370. https://doi.org/10.2151/jmsj.2016-019.
Granger, C.W.J., 1969. Investigating causal relations by econometric models and cross-spectral methods. Econometrica 37 (3):424–438. https://doi.org/10.2307/1912791.
Guo, D., Wang, L., Li, Z., et al., 2016. Comparison between anomalies of summer rainfall in China in decaying years during super El Niño events of 2015/2016 and 1997/1998. Trans. Atmos. Sci. 835–844 (in Chinese).
Hanley, D.E., Bourassa, M.A., O'Brien, J.J., Smith, S.R., Spade, E.R., 2003. A quantitative evaluation of ENSO indices. J. Clim. 16, 1249–1258.
Hargreaves, G.H., ASCE, F., Allen, R.G., 2003. History and evaluation of Hargreaves evapotranspiration equation. J. Irrig. Drain. Eng. 129, 53–63.
Huggins, L.F., Monke, E.J., 1966. The mathematical simulation of the hydrology of small watersheds. IWRRC Tech. Rep. No. 1. Purdue University Water Resource Research Center West, Lafayette, Indiana, pp. 26–80.
Hutchinson, M.F., 1998a. Interpolation of rainfall data with thin plate smoothing splines - part I: two dimensional smoothing of data with short range correlation. J. Geogr. Inf. Decis. Anal. 2 (2), 139–151.
Hutchinson, M.F., 1998b. Interpolation of rainfall data with thin plate smoothing splines - part II: analysis of topographic dependence. J. Geogr. Inf. Decis. Anal. 2 (2), 152–167.
Jiang, B., Liang, S., Yuan, W., 2015. Observational evidence for impacts of vegetation change on local surface climate over northern China using the Granger causality test. J. Geophys. Res. Biogeosci. 120:1–12. https://doi.org/10.1002/2014JG002741.
Jin, D., Hameed, S.N., Huo, L., 2016. Recent changes in ENSO teleconnection over the western Pacific impacts the Eastern China precipitation dipole. J. Clim. 29 (21), 7587–7598.
Kogan, F., Guo, W., 2017. Strong 2015–2016 El Niño and implication to global ecosystems from space data. Int. J. Remote Sens. 38 (1), 161–178.
Lau, K.M., Weng, H., 2001. Coherent modes of global SST and summer rainfall over China: an assessment of the regional impacts of the 1997–98 El Niño. J. Clim. 14 (6): 1294–1308. https://doi.org/10.1175/1520-0442(2001)014<1294:CMOGSA>2.0.CO;2.
Li, C., Ma, H., 2012. Relationship between ENSO and winter rainfall over Southeast China and its decadal variability. Adv. Atmos. Sci. 29 (6), 1129–1141.
Li, W., Zhai, P., Cai, J., 2011. Research on the relationship of ENSO and the frequency of extreme precipitation events in China. Adv. Clim. Chang. Res. 2 (2):101–107. https://doi.org/10.3724/SP.J.1248.2011.00101.
Lim, Y.K., Kovach, R.M., Pawson, S., Vernieres, G., 2017. The 2015/2016 el Niño event in context of the MERRA-2 reanalysis: a comparison of the tropical Pacific with 1982/1983 and 1997/1998. J. Clim. https://doi.org/10.1175/JCLI-D-16-0800.1.
Lin, B., Xia, L., Xie, H., 2013. Application of autoregressive model for low flow prediction. J. Water Resour. Res. 2, 222–227 (in Chinese).
Mao, Y., Ye, A., Liu, X., et al., 2016. High-resolution simulation of the spatial pattern of water use in continental China. Hydrol. Sci. J. https://doi.org/10.1080/02626667.2016.1153102.
NCCCMA (National Climate Committee of the China Meteorological Administration), 2016. The Press Conference of China Meteorological Administration. (in Chinese). http://www.cma.gov.cn/2011wmhd/2011wzbft/index_588_1.html.
Nie, Y., Sun, L., Li, Q., Ma, L., 2016. Possible causes for the warmer and wetter autumn in 2015 in China. Meteorol. Monogr. 42 (4), 507–513 (in Chinese).
NOAA National Centers for Environmental Information (NCEI), 2016. State of the Climate: Drought for Annual 2015. (2016-01-13) [2016-05-08]. https://www.ncdc.noaa.gov/sotc/drought/201513.
Null, J., 2015. Which El Niño Index Is Best?. Weather and Climate Blog. https://ggweather.posthaven.com/which-el-nino-index-is-best
Ouyang, W., Gao, X., 2017. Farmland shift due to climate warming and impacts on temporal-spatial distributions of water resources in a middle-high latitude agricultural watershed. J. Hydrol. 547C, 156–167.
Ouyang, R., Liu, W., Fu, G., Liu, C., Hu, L., Wang, H., 2014. Linkages between ENSO/PDO signals and precipitation, streamflow in China during the last 100 years. Hydrol. Earth Syst. Sci. 18, 3651–3661.
Ouyang, W., Liu, B., Huang, B., 2015. Watershed water circle dynamics during long term farmland conversion in freeze-thawing area. J. Hydrol. 523, 555–562.
Paek, H., Yu, J.-Y., Qian, C., 2017. Why were the 2015/16 and 1997/98 extreme El Niños different? Geophys. Res. Lett. https://doi.org/10.1002/2016GL071515.
Pereira, L., Pereira, A., Allen, R., Alves, I., 1999. Evapotranspiration: concepts and future trend. J. Irrig. Drain. Eng. 4:45–51. https://doi.org/10.1061/(ASCE)0733-9437(1999).
Raziei, T., Pereira, L.S., 2013. Estimation of ETo with Hargreaves–Samani and FAO-PM temperature methods for a wide range of climates in Iran. Agric. Water Manag. 121 (0), 1–18.
Ren, H.L., Wang, R., Zhai, P., Ding, Y., Lu, B., 2017. Upper-ocean dynamical features and prediction of the super El Niño in 2015/16: a comparison with the cases in 1982/83 and 1997/98. J. Meteor Res. 31 (2), 278–294.
Schwarz, G., 1978. Estimating the dimension of a model. Ann. Stat. 6 (2), 461–464.
Shao, X., Liu, Y., Li, D., 2015. Main characteristics and possible causes for the climate in China in spring 2015. Meteorol. Monogr. 41 (10), 1292–1297 (in Chinese).
Sun, Q., Miao, C., AghaKouchak, A., et al., 2016. Century-scale causal relationships between global dry/wet conditions and the state of the Pacific and Atlantic Oceans. Geophys. Res. Lett. 43 (12):6528–6537. https://doi.org/10.1002/2016GL069628.

Trenberth, K.E., Branstator, G.W., Karoly, D., Kumar, A., Lau, N., Ropelewski, C., 1998. Progress during TOGA in understanding and modeling global teleconnections associated with tropical sea surface temperature. J. Geophys. Res. Ocean 103:291–324. https://doi.org/10.1029/97JC01444.
Wang, N., Zhang, Y., 2015. Evolution of Eurasian teleconnection pattern and its relationship to climate anomalies in China. Clim. Dyn. 44 (3–4), 1017–1028.
Wang, B., Wu, R., Fu, X., 2000. Pacific–East Asia teleconnection: how does ENSO affect East Asian climate? J. Clim. 13, 1517–1536.
Wang, B., Wu, R., Lau, K.-M., 2001. Interannual variability of the Asian summer monsoon: contrasts between the Indian and the Western North Pacific–East Asian monsoons. J. Clim. 14, 4073–4090.
Wang, S., Zhang, Y., Feng, J., 2015. Drought events and its influence in summer of 2015 in China. J. Arid Meteor. 33 (5), 888–893 (in Chinese).
WMO, 2009. WMO El Niño/La Niña updates. http://www.wmo.int/pages/prog/wcp/wcasp/documents/El_Nino_Aug09_Eng.pdf.
WMO, 2016. WMO El Niño/La Niña updates archive. (2015-11-16). http://www.wmo.int/pages/prog/wcp/wcasp/enso_updates.html.
Wright, W., 2014. Discussion paper on the calculation of the standard climate normals: a proposal for a dual system. World Climate Data and Monitoring Program, Accessed, 14.
Wu, R., Wang, B., 2002. A contrast of the East Asian summer monsoon–ENSO relationship between 1962–77 and 1978–93. J. Clim. 15 (22), 3266–3279.
Wu, R., Hu, Z.Z., Kirtman, B.P., 2003. Evolution of ENSO-related rainfall anomalies in East Asia. J. Clim. 16 (22):3742–3758. https://doi.org/10.1175/1520-0442(2003)016<3742:EOERAI>2.0.CO;2.
Wu, L., Wang, Y., Qiao, L., Du, L., Qiu, L., 2016. Analysis of rainfall anomalies in China in April 2015. J. Anhui Agri. Sci. 44 (9), 216–220 (in Chinese).
Xia, J., Wang, G., Lv, A., 2003. A research on distributed time variant gain modeling. Acta Geograph. Sin. 58 (5):789–796. https://doi.org/10.11821/xb200305019.
Xia, J., Wang, G., Tan, G., Huang, H., 2005. Development of distributed time-variant gain model for nonlinear hydrological systems. Sci. China. Ser. D Earth Sci. 48 (6):713–723. https://doi.org/10.1360/03yd0183.
Xiao, Y., Du, Y., Du, L., 2016. Oceanic and atmospheric circulation anomalies in 2015 and 2016 and their impacts on summer precipitation in China. J. Nat. Res. 31 (12), 1995–2004.
Xie, S.-P., Hu, K., Hafner, J., Tokinaga, H., Du, Y., Huang, G., Sampe, T., 2009. Indian Ocean capacitor effect on indo–western Pacific climate during the summer following El Nino. J. Clim. 22, 730–747.
Xu, J., Chen, Y., Li, W., 2014. The nonlinear hydro-climatic process: a case study of the Tarim headwaters, NW China. In: Chen, Y. (Ed.), Water Resources Research in Northwest China. Springer, Dordrecht, pp. 289–310.
Ye, A., Duan, Q., Zeng, H., Li, L., Wang, C., 2010. A distributed time-variant gain hydrological model based on remote sensing. J. Resour. Ecol. 1 (3):222–230. https://doi.org/10.3969/j.issn.1674-764x.2010.03.005.
Yu, J.-Y., Kim, S.T., 2013. Identifying the types of major El Niño events since 1870. Int. J. Climatol. 33, 2105–2112.
Yuan, Y., Yang, S., 2012. Impacts of different types of El Niño on the East Asian climate: focus on ENSO cycles. J. Clim. 25 (21):7702–7722. https://doi.org/10.1175/JCLI-D-11-00576.1.
Yuan, Y., Gao, H., Jia, X., Wan, J., 2016. Influences of the 2014–2016 super El Niño event on climate. Meteorol. Monogr. 42 (5), 532–539 (in Chinese).
Yuan, Y., Gao, H., Li, W., et al., 2017. The 2016 summer floods in China and associated physical mechanisms: a comparison with 1998. J. Meteor. Res. 31 (2), 261–277.
Zhai, P., Yu, R., Guo, Y., et al., 2016. The strong El Niño of 2015/16 and its dominant impacts on global and China's climate. J. Meteor. Res. Appl. 30 (3), 283–297.
Zhang, R., 2001. Relations of water vapor transport from Indian monsoon with that over East Asia and the summer rainfall in China. Adv. Atmos. Sci. 18 (5), 1005–1017.
Zhang, R., Sumi, A., Kimoto, M., 1996. Impact of El Niño on the East Asian monsoon: a diagnostic study of the 86/87 and 91/92 events. J. Meteorol. Soc. Jpn. 74 (1), 49–62.
Zhang, R., Sumi, A., Kimoto, M., 1999. A diagnostic study of the impact of El Nino on the precipitation in China. Adv. Atmos. Sci. 16 (2):229–241. https://doi.org/10.1007/BF02973084.
Zhao, Y., Shen, L., 2011. Application of time series auto regressive model in price forecast. Business Management and Electronic Information (BMEI). 2011 International Conference on IEEE. 4, pp. 768–771.